Contents lists available at ScienceDirect

Solar Energy

The influence of perovskite precursor composition on the morphology and photovoltaic performance of mixed halide MAPbI$_{3-x}$Cl$_x$ solar cells

Sekai Tombe[a,b], Getachew Adam[b,*], Herwig Heilbrunner[b], Cigdem Yumusak[b],
Dogukan Hazar Apaydin[b], Bekele Hailegnaw[b], Christoph Ulbricht[b], Christopher J. Arendse[c],
Heinz Langhals[b], Emmanuel Iwuohaa[c], Niyazi Serdar Sariciftci[b], Markus C. Scharber[b]

[a] SensorLab, Department of Chemistry, University of the Western Cape, Robert Sobukwe Road, Bellville, 7535 Cape Town, South Africa
[b] Linz Institute for Organic Solar Cells (LIOS), Institute of Physical Chemistry, Johannes Kepler University Linz, Altenbergerstrasse 69, 4040 Linz, Austria
[c] Department of Physics, University of the Western Cape, Private Bag X17, Bellville, 7535 Cape Town, South Africa

ARTICLE INFO

ABSTRACT

A set of various perovskite precursor formulations was investigated to elucidate correlations between precursor composition and the crystal structure, film morphology as well as photovoltaic activity of H$_3$CNH$_3$PbI$_{3-x}$Cl$_x$ perovskite solar cells. Three precursor solutions in dimethylfromamide (DMF) with defined ratios of lead(II) halide (PbI$_2$ and/or PbCl$_2$) and methylammonium halide (H$_3$CNH$_3$I (MAI) and H$_3$CNH$_3$Cl (MACl)) such as 1:3 (PbCl$_2$:MAI), 1:1:4 (PbI$_2$:PbCl$_2$:MAI) and 1:1:1 (PbI$_2$:MAI:MACl) were used to prepare solar cells in primarily ambient atmosphere. Processing the 1:3 (PbCl$_2$:MAI) solution in ambient atmosphere yielded perovskite films with rather non-uniform morphology and devices with moderate performance. Perovskite thin films prepared from the 1:1:4 (PbI$_2$:PbCl$_2$:MAI) and 1:1:1 (PbI$_2$:MAI:MACl) formulation showed nearly identical features, high crystallinity, large and compact micrometer-sized crystal domains, and good photovoltaic performance. This indicates that the overall ionic composition in the precursor solution is crucial for the perovskite formation, the source of these ions, however, appears nonrelevant. Furthermore, the effect of different electron transport layers (ETL), PCBM, *bis*-PCBM, and *N*-[4-(benzothiadiazol-4-yl)phenyl]-*N′*-(1-nonyldecyl)perylene-3,4,9,10-tetra-carboxdimide (a-PTCDI) on the photovoltaic performance was analyzed. The highest hysteresis-free power conversion efficiency (PCE) was achieved with PCBM (12.8%) followed by a-PTCDI (8.4%) and *bis*-PCBM (6%). The degradation of MAPbI$_{3-x}$Cl$_x$ based devices stored in nitrogen atmosphere was primarily revealed by a loss in fill factor.

1. Introduction

Organic-inorganic lead halide perovskites have emerged as high-performance photovoltaic materials and show great potential for next generation photovoltaic technology due to their high efficiency and low cost of fabrication (Burschka et al., 2013; Kim et al., 2012; Lee et al., 2012; M. Yang et al., 2015; W.S. Yang et al., 2015). These perovskites with appealing optoelectronic features are commonly prepared from organic halide and metal halide salts to form crystals in the perovskite ABX$_3$ structure comprising of organic and/or metal mono cation A, a divalent metal cation B, and halide anions X. Solution-processability and, compatibility with large-area deposition techniques, inexpensive base materials and desirable characteristics such as bandgap tunability, (Noh et al., 2013) high open-circuit voltage (V$_{oc}$), (Correa Baena et al., 2015) strong light absorption with high absorption coefficients (Kojima

et al., 2012, Löper et al., 2015) and high carrier mobility (Kagan et al., 1999; Mitzi et al., 1995) make this class of material very attractive for solar energy conversion. Additionally, ambipolar carrier transport within lead halide perovskites further highlights the unique excited state character of this special group of semiconductors (Etgar et al., 2012; Cui et al., 2017; Ke et al., 2015; Mei et al., 2014; Zhang et al., 2016).

The fabrication processes available for perovskites are robust and a myriad of approaches has been developed to deposit perovskite films. Perovskite solar cells can be processed using various techniques such as spin coating, (Lee et al., 2012) dip coating (Burschka et al., 2013), two-step interdiffusion (Xiao et al., 2014), chemical vapor deposition, (Chen et al., 2014) spray deposition, (Barrows et al., 2014) atomic layer deposition, (Sutherland et al., 2015) ink-jet printing (Wei et al., 2014) and thermal evaporation (Liu et al., 2013; Malinkiewicz et al., 2014)

making them one of the most versatile photovoltaic (PV) technologies and potentially enables large flexibility in device design at low fabrication cost. A remarkable feature of the organic-inorganic halide perovskite system is the tunability of the crystal lattice dimensions through cation and/or anion variation, which defines the bandgap of these absorbers. Recent examples are the use of formamidinium cations (FA, $HC(NH_2)_2^+$) and of alternative halides. (Eperon et al., 2014a; Lee et al., 2015; Saliba et al., 2016; Yang et al., 2016) While pure perovskite compounds such as $MAPbX_3$, $FAPbX_3$ and $CsPbX_3$ (MA = $H_3CNH_3^+$, X = I^-, or Br^-) showed numerous short comings, formulations based on mixed cations and halides yielded perovskite compounds with improved power conversion efficiency (PCE) as well as structural and thermal stability of the solar cell devices (Heo and Im, 2016; Jeon et al., 2015; Nie et al., 2015; Noh et al., 2013).

Understanding how to control the transformation from precursor solution into solid semiconductor is critical to produce high performance perovskite devices (Manser et al., 2016). Even in the relatively simple case of $MAPbX_3$ (X = I^-, Br^-, or Cl^-) precursor solutions, aside from the chosen halide (Lee et al., 2012; Stranks et al., 2013; Zhao and Zhu, 2014) variations in the solvent (Jeon et al., 2014; Kim et al., 2014), stoichiometry of the components (Manser et al., 2015; M. Yang et al., 2015; W.S. Yang et al., 2015), processing atmosphere (Ko et al., 2015; You et al., 2014), annealing temperature and time (Eperon et al., 2014b; Saliba et al., 2014) can affect the morphology and optoelectronic properties of the resulting film distinctively. Hence, it is of great significance to explore new processes for low-temperature fabrication of organic-inorganic perovskites and provide a better understanding of some fundamental physical and chemical properties of these materials. To date all high-efficiency perovskite solar cells reported make use of formulations based on mixed cations and halides (Jeon et al., 2015).

Another common feature of such high-performance perovskite-based solar cells is the integration of mesoscopic metal oxide interlayers such as Al_2O_3, TiO_2 or ZrO_2 with an expense of high-temperature sintering process. Such a high temperature processes, however, are usually not compatible with low-cost, lightweight and flexible plastic substrates (Docampo et al., 2013; Roldán-Carmona et al., 2014; Sun et al., 2014) and multi-junction device architectures (Bailey and McGehee, 2012). Substitution of the metal oxide layers by organic semiconductors can help to overcome such obstacles and to simplify the fabrication of devices.

To enhance exciton separation, charge transportation and collection, the deposition of a conformal and chemically inert electron transport layer (ETL) on top of the perovskite film to complement the underlying hole transport layer appears essential for the fabrication of high-efficient planar heterojunction perovskite solar cells (Yin et al., 2016). Reports on polymer-based bulkheterojunction solar cells showed the use of *bis*-PCBM instead of PCBM can lead to an increase in V_{oc}, which is attributed to its significant higher lowest unoccupied molecular orbital (LUMO) level. (Han et al., 2016; He and Li, 2011; Lenes et al., 2008). Perylenetetracarboxylic diimides (PTCDIs), originally developed as pigments with high resistance to degradation, are used as non-fullerene acceptors due to their n-type properties and the vast possibilities of structural modifications to tune their optoelectronic and morphological features (Huang et al., 2011; Zhan et al., 2011). Kaltenbrunner et al. (2015), reported efficient planar heterojunction $MAPbI_{3-x}Cl_x$ solar cells using N,N'-dimethyl-3,4,9,10-tetracarboxylic perylene diimide, thermally deposited in vacuum, as an electron transporting material. In addition to this, the stability of perovskite based devices remains an open question and perhaps will determine the fate of these promising materials for technological application in the long run.

In this work, we investigate the straightforward fabrication of planar p-i-n heterojunction perovskite solar cells, (ITO/PEDOT:PSS/perovskite/ETL/Al), excluding high temperature processing steps and using almost exclusively solution-processing techniques in ambient atmosphere. As a first objective, three different $MAPbI_{3-x}Cl_x$ perovskite

precursor compositions, 1:3 ($PbCl_2$:MAI), 1:1:1 (PbI_2:MAI:MACl) and 1:1:4 (PbI_2:$PbCl_2$:MAI) dissolved in dimethylformamide (DMF), were investigated regarding their conversion into perovskite thin films in ambient atmosphere. Using identical processing procedures the emphasis of the study is on the composition of the three precursors formulations. While 1:1:4 and 1:1:1 use in parts different base components, the overall composition of ions in the two precursor formulations is identical (Pb^{2+}:MA^+:I^-:Cl^- = 1:2:3:1). In the precursor formulation 1:3 (Pb^{2+}:MA^+:I^-:Cl^- = 1:3:3:2) the content of the excessive MACl is twice as high. The morphology and crystallinity of the obtained perovskite films were investigated by means of scanning electron microscopy (SEM), atomic force microscopy (AFM) and X-ray diffraction (XRD), respectively. The solar cell performance was investigated by current density-voltage and external quantum efficient measurements. The processing of 1:3 ($PbCl_2$:MAI) in ambient air resulted in poor film morphology and was found to be detrimental to the perovskite crystal structure. In contrast we found substantial better and nearly identical morphology and crystallinity, as well as performance in the perovskite films obtained from the 1:1:1 (PbI_2:MAI:MACl) and the 1:1:4 (PbI_2:$PbCl_2$:MAI) precursor formulations. Another critical element in our device layout was the deposition of an inert electron-transporting layer (ETL). We probed three electron-transport materials, *bis*-PCBM, PCBM and an amorphous PTCDI derivative (a-PTCDI) simply deposited from solution at room temperature. The best performing planar perovskite solar cells employing PCBM, a-PTCDI and *bis*-PCBM as electron transport materials achieved power conversion efficiency of 12.8, 8.4 and 6%, respectively. Solar cells which were obtained from the 1:1:1 (PbI_2:MAI:MACl) formulation showed good shelf stability in nitrogen-filled glove box.

2. Experimental

2.1. Materials

Chemicals and solvents were purchased from commercial suppliers and used as received, if not stated otherwise. Pre-patterned indium doped tin oxide (ITO) coated glass (15 Ohm/cm^2), PbI_2 (99.9%, Sigma Aldrich), $PbCl_2$ (99.9%, Sigma Aldrich), dimethylformamide (DMF, anhydrous, Sigma Aldrich), poly(3,4-ethylenedioxythiophene) polystyrene sulfonate (PEDOT:PSS, Clevios PH 1000), Zonyl®FS-300 fluorosurfactant (40% in H_2O, Fluka), dimethyl sulfoxide (DMSO, AnalR, VWR Chemicals), [6,6]-phenyl-C_{61}-butyric acid methyl ester (PCBM; SolenneBV), *bis*-adduct of phenyl-C_{61}-butyric acid methyl ester (mixtures of isomers, *bis*-PCBM, SolenneBV), chlorobenzene (GPR, VWR Chemicals), chloroform (AnalR, VWR Chemicals), isopropanol (AnalR, Fisher Chemicals) and methylammonium chloride (MACl, MERCK) were used as received. Methylamine (33 wt%, in absolute ethanol, Sigma Aldrich), hydroiodic acid (57 wt%, aqueous, Riedel de Haën), diethyl ether (VWR Chemicals), and ethanol (absolute, MERCK) were used to synthesize and purify methylammonium iodide (MAI) according to literature (Burschka et al., 2013). N-[4-(benzothiadiazol-4-yl)phenyl]-N'-(1-nonyldecyl)perylene-3,4,9,10-tetracarboxdimide (IUPAC: (2-[4-(2,1,3-benzothiadiazol-4-yl)phenyl]-9-(1-nonyldecyl)anthra[2,1,9-*def*:6,5,10-*d'e'f'*]diisoquinoline-1,3,8,10(2H,9H)-tetrone; registry number 1417610-38-8) an amorphous PTCDI derivative, in here abbreviated as a-PTCDI, was synthesized according to literature (Langhals et al., 2012).

2.2. Perovskite precursor solutions

$MAPbI_{3-x}Cl_x$ perovskite precursor formulations of 0.8 M concentration were prepared by dissolving defined molar ratios of lead halides and methylammonium halides, 1:3 ($PbCl_2$:MAI), 1:1:4 (PbI_2:$PbCl_2$:MAI) and 1:1:1 (PbI_2:MAI:MACl), in DMF. To ensure a complete dissolution the mixtures were stirred overnight at room temperature. The solutions were filtered through a PTFE syringe filter (0.45 µm) before use.
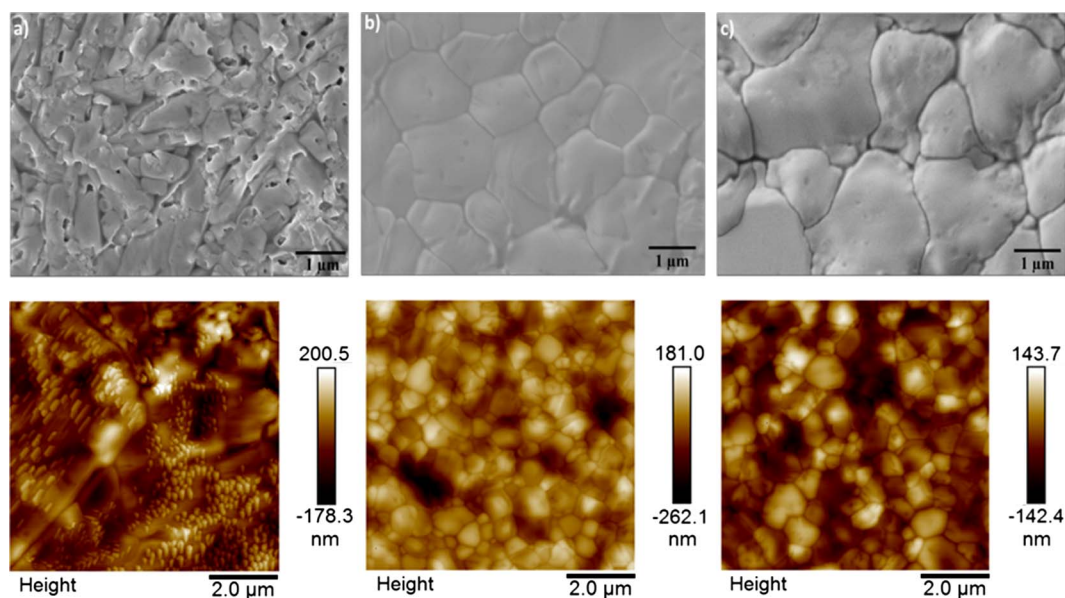
Fig. 1. SEM (*top*) and AFM (tapping mode scan, *bottom*) images of perovskite films on glass/ITO/PEDOT:PSS substrates obtained with different precursor solutions (a) 1:3 ($PbCl_2$:MAI), (b) 1:1:4 (PbI_2:$PbCl_2$:MAI) and (c) 1:1:1 (PbI_2:MAI:MACl), spin coated and annealed in ambient atmosphere.

2.3. Device fabrication and characterization

Planar heterojunction perovskite solar cells were prepared with a layer configuration of ITO/PEDOT:PSS/perovskite/ETL/Al using almost exclusively solution processing (spin coating) in ambient atmosphere. The glass/ITO substrates were cleaned successively with acetone and isopropanol in an ultrasonic bath. The Clevious PH 1000 PEDOT:PSS dispersion was mixed with DMSO (5 vol%) and Zonyl (0.7 vol%), and filtered through regenerated cellulose (RC) syringe filter (0.45 μm), before spin coating (1000 rpm for 1 min) on top of ITO. This was followed by annealing (heating plate at 110 °C for 10 min), rinsing with isopropanol, and another 10 min annealing at 110 °C (Adam et al., 2016). Subsequently the perovskite precursor solution, $MAPbI_{3-x}Cl_x$, was deposited by spin coating (1800 rpm for 15 s and 2000 rpm for 5 s). The transformation of the perovskite layer was completed by annealing at 110 °C for 45 min. On top of the perovskite film an ETL was deposited from solution. For PCBM and *bis*-PCBM (20 mg/ml in chlorobenzene/chloroform (1:1 by volume)) spin coating (1500 rpm for 30 s) was performed. After the wet processing steps the substrates were loaded into a glove box (N_2 atmosphere), and the aluminum contacts were thermally deposited in a vacuum chamber (4×10^{-6} mbar). The completed photovoltaic devices were kept in inert atmosphere (N_2) for the following characterizations. For photoluminescence (PL) quenching experiments perovskite films were fabricated on cleaned and O_2-plasma-treated glass substrates using the precursor formulation 1:1:4 (PbI_2:$PbCl_2$:MAI). ETL materials, PCBM, *bis*-PCBM and a-PTCDI, were deposited on top to investigate the impact on the photoluminescence of the perovskite layer. To measure charge carrier mobility of a-PTCDI, organic field effect transistor (OFET) devices were fabricated by drop casting a-PTCDI from its solution in chlorobenzene in a bottom-gate, bottom-contact geometry on heavily doped Si wafers (Fraunhofer IPMS), consisting of a 90 nm SiO_2 layer integrated with 30 nm thick Au source drain electrodes on a 10 nm ITO adhesion layer.

To test the fabricated solar cells under standardized light irradiation (AM1.5G) a LOT-QD solar simulator (LS0821) was used. The intensity of radiation was adjusted to 100 mW/cm^2 using a calibrated reference silicon diode (Hamamatsu S2281). Current density–voltage curves were recorded with a Keithley 2400 source-measurement unit in dark and under illumination. To check for hysteresis, current density–voltage scans were performed in both, forward and reverse direction, at a rate of 20 mV/s. External quantum efficiencies (EQEs) were recorded by

using a lock-in amplifier (SR830, Stanford Research Systems) and a Jaissle 1002 potentiostat functioning as a preamplifier. The devices were illuminated by light from a xenon lamp passing through a monochromator (Oriel Cornerstone). A filter wheel holding long-pass filters and a mechanical chopper was mounted between the Xenon lamp and the monochromator. Chopping frequencies in the range of 10–200 Hz were used. X-ray diffraction measurements were conducted in ω/2θ geometry using a Bruker AXS diffractometer with Fe Kα irradiation. Surface and cross section scanning electron microscopy (SEM) measurements were carried out using a ZEISS 1540XB cross beam scanning electron microscope equipped with an energy dispersive X-ray spectroscopy (EDX) unit. Furthermore, atomic force microscopy (AFM) measurements were conducted using a Bruker Innova to record surface morphologies and to characterize the roughness of perovskite films. A photoluminescence (PL) setup consisting of a coherent UV GaN-based laser (VIOFLAME 405 nm/25 mW), a Shamrock SR-303i monochromator, and an Andor™ iDus Si-CCD detector was utilized for PL quenching experiments. The charge mobility measurements at OFETs were conducted using an EverBeing mini probe station in a nitrogen-filled glove box and an Agilent B1500A semiconductor parameter analyzer.

3. Results and discussion

3.1. Perovskite thin film morphology

In this work, a one-step fabrication protocol in ambient atmosphere is used to cast perovskite films from different precursor solutions with organic (MAI and/or MACl) and inorganic (PbI_2 and/or $PbCl_2$) components. Subsequent annealing drives the formation of the perovskite phase towards completion. The morphology of the films obtained from the $MAPbI_{3-x}Cl_x$ precursor solutions, 1:3 ($PbCl_2$:MAI), 1:1:1 (PbI_2:MAI:MACl) and 1:1:4 (PbI_2:$PbCl_2$:MAI), were investigated by scanning electron microscopy (SEM) and atomic force microscopy (AFM). Recorded images are depicted in Fig. 1.

The morphologies of the $MAPbI_{3-x}Cl_x$ crystallites (Fig. 1), obtained under the given processing conditions, is massively affected by the fraction of volatile MACl evolving during the formation of the $MAPbI_3$-dominated perovskite films. The 1:3 $PbCl_2$:MAI precursor, known to yield high performance when processed in inert atmosphere (Ke et al., 2015; Heo and Im, 2016) gave a film with non-uniform perovskite

morphology upon spin coating and annealing in air (Fig. 1a). The film casted from the 1:3 formulation appeared extremely moisture sensitive until the crystallization had finalized. The poor surface morphology is likely to affect charge transport and extraction unfavorably. In comparison to 1:3 (PbCl$_2$:MAI) the perovskite films prepared from 1:1:4 (PbI$_2$:PbCl$_2$:MAI) (Fig. 1b) and 1:1:1 (PbI$_2$:MAI:MACl) (Fig. 1c) exhibit the same appearance with nicely dense micron-sized perovskite crystal domains. The morphological differences are also reflected in the roughness of the perovskite films. The root-mean square (RMS) roughness, determined by AFM, is almost identical for the films from the 1:1:4 (PbI$_2$:PbCl$_2$:MAI) and the 1:1:1 (PbI$_2$:MAI:MACl) perovskite precursor formulation, about 42 nm. With 53 nm the RMS roughness of the film casted from the 1:3 (PbCl$_2$:MAI) formulation is significantly higher. While apparently changes in the overall ionic composition of the precursor solution can impact the perovskite film formation dramatically, the original source of the ions (*via* organic or inorganic salts) seems not to matter. Recent and previous reports confirm that the addition of Cl$^-$ to the system via either MACl or PbCl$_2$ modifies the crystallization pathway from precursor-perovskite to precursor-intermediate-perovskite and dramatically changes kinetics of crystallization (Stranks et al., 2013; Zhao and Zhu, 2014).

To probe if the difference in morphology between 1:3 (PbCl$_2$:MAI) films (Fig. 1a), and the films obtained from either the 1:1:4 (PbI$_2$:PbCl$_2$:MAI) (Fig. 1b) or the 1:1:1 (PbI$_2$:MAI:MACl) formulation (Fig. 1c) might be rooted in variations in their crystal structure, X-ray diffraction spectroscopy (XRD) measurements were carried out. MAPbI$_{3-x}$Cl$_x$ perovskite films were spin-coated on glass/ITO/PEDOT:PSS substrates. Fig. 2 presents the XRD patterns of perovskite films deposited from 1:3 (PbCl$_2$:MAI) and 1:1:1 (PbI$_2$:MAI:MACl) precursor solution. Characteristic perovskite diffraction peaks at about 15.4°, 29.5° and 43.4° can be assigned to (1 1 0), (2 2 0) and (3 3 0) planes of crystalline MAPbI$_{3-x}$Cl$_x$, respectively.

X-ray diffraction evidences the formation of a tetragonal perovskite phase (Poglitsch and Weber, 1987) in agreement with previously reported XRD data (Kim et al., 2016; Liang et al., 2014; Liu et al., 2013). There are no apparent peaks corresponding to unreacted PbI$_2$ or PbCl$_2$ indicating no secondary phase and suggesting complete transformation of PbI$_2$ and PbCl$_2$ into perovskite (Liu et al., 2013). The increased intensity of the [1 1 0] and [2 2 0] peaks in the case of 1:1:1 (PbI$_2$:MAI:MACl) precursor indicates preferential orientation of these planes parallel to the substrate surface. This shows that though the crystal structures are similar their growth and orientation on the substrate is different as can be seen in the SEM images in Fig. 1.
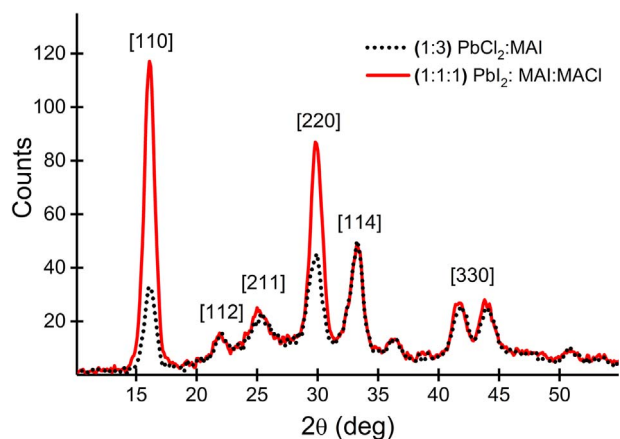

Fig. 2. X-ray diffraction (XRD) spectrum of a MAPbI$_{3-x}$Cl$_x$ film prepared by spin-coating of the precursor solutions 1:3 (PbCl$_2$:MAI) (*black dotted line*) and 1:1:1 (PbI$_2$:MAI:MACl) (*red solid line*) on a glass/ITO/PEDOT:PSS substrate and annealing at 110 °C. (For interpretation of the references to colour in this figure legend, the reader is referred to the web version of this article.)

3.2. Photovoltaic characterization

3.2.1. Current density-voltage (J-V) characteristics and external quantum efficiencies (EQE)

The two ion compositions, Pb^{2+}MA$^+$3I$^-$2MA$^+$2Cl$^-$ (precursor solutions 1:3) and Pb^{2+}MA$^+$3I$^-$ MA$^+$Cl$^-$ (precursor solutions 1:1:4 and 1:1:1), processed under identical conditions produce a different perovskite morphology (grain size/shape, film roughness and surface coverage). The differences in crystallization impact the photovoltaic performance in the final devices. The J-V curves of the best-performing solar cells as well as the corresponding external quantum efficiencies (EQE) are depicted in Fig. 3. All the three precursor compositions allowed the fabrication of diodes with excellent rectification and low-reverse-bias dark currents (Fig. S1). The device characteristics of 1:1:4 (PbI$_2$:PbCl$_2$:MAI) and 1:1:1 (PbI$_2$:MAI:MACl), show high resemblance, V$_{oc}$ ~ 950 mV, J$_{sc}$ ~ 17 mA/cm^2 (EQE), FF ~ 0.76, PCE ~ 12.7%, which appears to reflect the analogies in the ion composition and the obtained film morphologies.

Power conversion efficiencies of about ~18% have been reported for devices based on 1:3 (PbCl$_2$:MAI) formulation, if the fabrication was conducted in a dry nitrogen atmosphere. The processing of the 1:3 (PbCl$_2$:MAI) perovskite precursor solution in ambient air, however, was found to be detrimental to the device performance V$_{oc}$ = 900 mV, J$_{sc}$ = 15.7 mA/cm^2 (EQE), FF = 0.54, and PCE = 7.8%, (Fig. 3c,d). The small grain sizes in case of 1:3 (PbCl$_2$:MAI) (Fig. 1a) increase the volume of grain boundaries, which can act as charge traps and facilitate trap assisted recombination within the perovskite layer, thereby limiting device efficiency. The higher crystallinity induces a better performance for the 1:1:1 (PbI$_2$:MAI:MACl) and the 1:1:4 (PbI$_2$:PbCl$_2$:MAI) derived devices. Large perovskite grains provide a favorable interface between the active layer and transport layers permitting photogenerated charges to be extracted through device electrodes without the need to pass through grain boundaries. Furthermore, the volume of grain boundaries in perovskite films with large crystallite grains is significantly reduced, which decreases the density of defects facilitating charge-recombination.

The overlaid EQE spectra of the 1:3 (PbCl$_2$:MAI), 1:1:1 (PbI$_2$:MAI:MACl) and 1:1:4 (PbI$_2$:PbCl$_2$:MAI), devices are shown in Fig. 3d. The absorption onset in EQE is identical regardless of the precursor composition indicating no change in bandgap. The EQE peaks for 1:1:1 (PbI$_2$:MAI:MACl) and 1:1:4 (PbI$_2$:PbCl$_2$:MAI) are reaching maxima (~80%) around 550 nm, whereas in case of 3:1 (MAI:PbCl$_2$) the trend is slightly different with a maximum plateau of about 68% in the range of 450–650 nm. In the blue (300–450 nm) and in the red (650–800 nm) the spectral response is substantially smaller leading to a significant reduction in photocurrent. This loss can be attributed to parasitic absorption in the ITO and PEDOT:PSS layer as well as the poor reflectance of the metal back aluminum electrode. The integrated short circuit currents from the EQE were determined to 15.6 mA/cm^2 for 3:1 MAI:PbCl$_2$ based device and 17.4 mA/cm^2 for the devices prepared from the other two precursors formulations, and matched well with the J$_{sc}$ values obtained from J-V curves under illumination. Power conversion efficiencies of 7.8, 12.5 and 12.9% were obtained for the 1:3 (PbCl$_2$:MAI), 1:1:4 (PbI$_2$:PbCl$_2$:MAI) and 1:1:1 (PbI$_2$:MAI:MACl) devices respectively. In general, no significant differences were observed, neither in morphology nor in the photovoltaic performance, for the solar cells fabricated from the 1:1:1 (PbI$_2$:MAI:MACl) and 1:1:4 (PbI$_2$:PbCl$_2$:MAI) precursor solution.

As 1:1:4 and 1:1:1 basically show identical characteristics and performance, only the formulations 1:1:1 and 1:3 were tested for hysteresis behavior. Fig. 4 shows that at a scan rate of 250 mV/s hysteresis is clearly evident for 1:3 (PbCl$_2$:MAI) (Fig. 4a) while it is negligible for the 1:1:1 (PbI$_2$:MAI:MACl) derived solar cells (Fig. 4b), demonstrating once again the significant impact of the precursor composition. The hysteresis in 1:3 (PbCl$_2$:MAI) gets even more pronounced with increasing scan rate (Fig. S2). The observed hysteresis behavior might
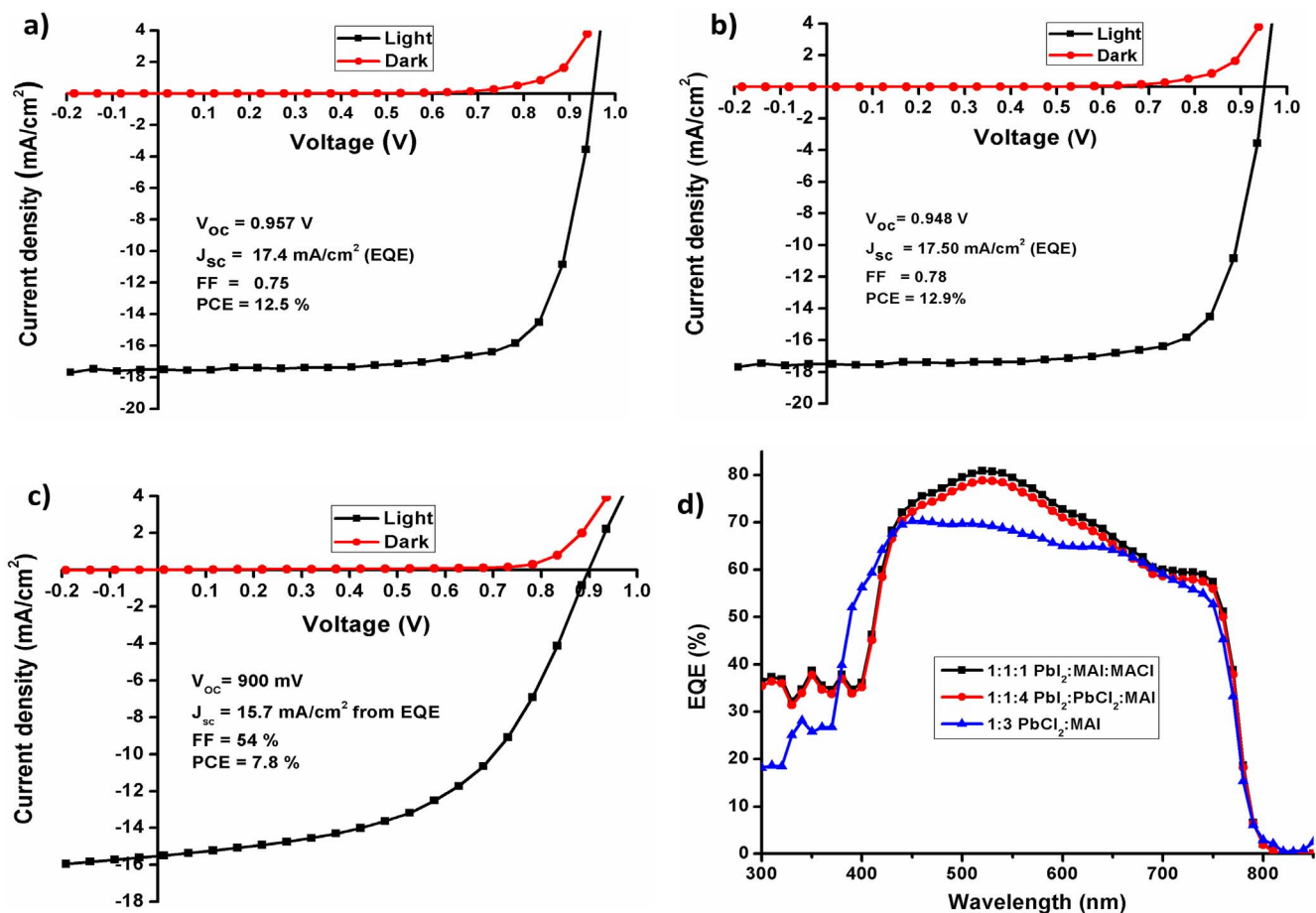
Fig. 3. Current density-voltage (J-V) characteristics recorded in dark and under illumination (AM1.5G), of the solar cells processed from (a) 1:1:4 (PbI_2:$PbCl_2$:MAI), (b) 1:1:1 (PbI_2:MAI:MACl) and (c) 1:3 ($PbCl_2$:MAI) as well as their corresponding EQE measurement (d).

also be a consequence of the differences in perovskite film morphology (Kim and Park, 2014, Kim et al., 2016). The observed defects and high number of crystal grain boundaries in the 1:3 ($PbCl_2$:MAI) perovskite layers might worsen the interface with the transport layers and act as traps of carriers causing the hysteresis. The observed hysteresis is an indication of poor electronic contact between perovskite and charge collection layer. Not only larger perovskite crystals but also the addition of a perovskite capping layer can reduce hysteresis (Ko et al., 2015). Small perovskite crystals and planar structures, on the other

hand, are supposed to accumulate charge and promote hysteresis (Jeon et al., 2015; Kim et al., 2016).

Fig. 5 shows the scanning electron microscopy cross-section of a $MAPbI_{3-x}Cl_x$ based device, glass/ITO/PEDOT:PSS/$MAPbI_{3-x}Cl_x$/PCBM/Al, fabricated from the 1:1:1 (PbI_2:MAI:MACl) precursor formulation. The individual layers with distinct features and contrast are visible, confirming the planar heterojunction architecture of the fabricated device. The perovskite absorber layer is well implemented into the device with intimate contact to adjacent layers – PEDOT:PSS at the
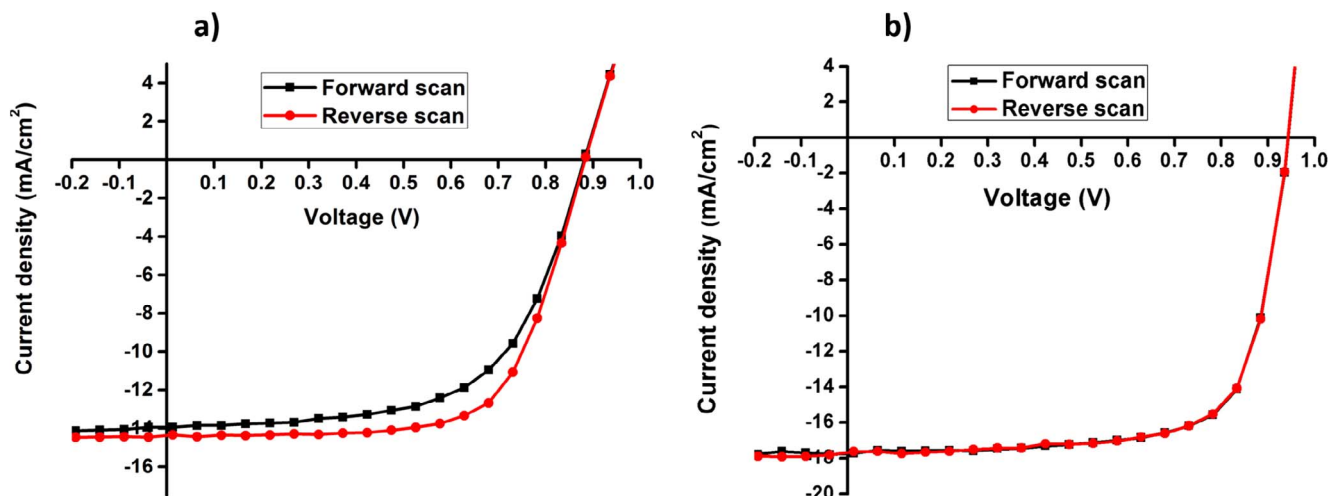

Fig. 4. Scan direction-dependent J-V curves of (a) 1:3 ($PbCl_2$:MAI) and (b) 1:1:1 (PbI_2:MAI:MACl) solar cells at a scan rate of 250 mV/s.
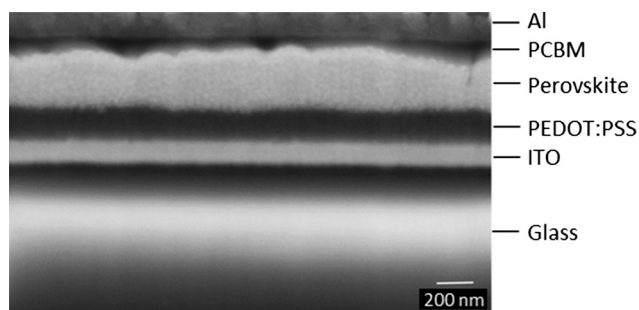
Fig. 5. Cross-sectional SEM image of MAPbI$_{3-x}$Cl$_x$ planar heterojunction perovskite solar cell fabricated from the 1:1:1 (PbI$_2$:MAI:MACl) precursor solution.

anode side and PCBM at the cathode side. The thickness of the PEDOT:PSS layer, the perovskite layer, the PCBM layer and the Al contact in the optimized device configuration, presented in this study, were 130, 350–400, 70, and 110 nm, respectively.

3.3. Effect of electron transport materials on the photovoltaic performance

Seeking further improvement in performance of devices processed from 1:1:1 (PbI$_2$:MAI:MACl) precursor, three potential electron transporting materials, PCBM, *bis*-PCBM and a-PTCDI were compared. The a-PTCDI investigated here is soluble in organic solvents, and forms amorphous films when processed from solution (Langhals et al., 2012). Moreover, its rather high LUMO level seems auspicious for achieving high open circuit voltage values. The energy level diagram of all device materials, and the chemical structures of the organic electron transport materials are shown in Fig. 6. The HOMO levels of PCBM, *bis*-PCBM and a-PTCDI are rather deep, −6.0, −6.1 (Ye et al., 2013) and −6.0 eV, (Huang et al., 2011) respectively, which is highly beneficial for effective hole-blocking.

The J-V curves as well as the EQE measurements of the investigated devices (Fig. 7) display distinct differences for the device performances. The photovoltaic parameters are summarized in Table 1. Devices without ETL fail to perform properly despite the reported ambipolar characteristics of organic-inorganic halide perovskites and their use as n-type transporters (Ball et al., 2013; Lee et al., 2012; Noh et al., 2013). Indeed, high efficiency electron acceptor-free perovskite solar cells (PCE ~ 14%) (Ke et al., 2015) have been reported. Our devices, however, use a low work function metal electrode (Al), which in direct contact with perovskite shows very poor performance. This suggests,

the PEDOT:PSS/MAPbI$_{3-x}$Cl$_x$ interface alone is apparently less efficacious in promoting exciton dissociation and charge transfer. All other devices with PCBM, *bis*-PCBM or a-PTCDI as ETL show typical photovoltaic behavior. The photovoltaic performance of the solar cells employing the different electron transport materials decreases in the order PCBM > a-PTCDI > *bis*-PCBM (Fig. 7, Table 1).

Compared to MAPbI$_{3-x}$Cl$_x$ perovskite (E$_{LUMO}$ = −3.75 eV) *bis*-PCBM and a-PTCDI possess only slightly lower LUMO levels, −3.8 and −3.9 eV, respectively. Such small differences in energy might hinder a highly-efficient electron transfer to the electrode. PCBM, on the other side, exhibits a much lower LUMO (−4.3 eV), which should ensure a quick electron transfer from the perovskite to PCBM. Negative effects such as electron accumulation and charge recombination at the interface, or even an electron back transfer from PCBM to the perovskite can be basically excluded. MAPbI$_{3-x}$Cl$_x$ devices employing PCBM exhibited the best performance and J-V characteristics; PCE of 12.8% with a V$_{oc}$ of 0.940 V, J$_{sc}$ of 17.92 mA/cm^2 and FF of 0.76, followed by the devices with a-PTCDI, and eventually the solar cells using *bis*-PCBM as ETL. Despite the rather high LUMO levels of *bis*-PCBM and a-PTCDI no enhancement in V$_{oc}$ or in any other photovoltaic parameters was observed in comparison with the PCBM-based devices (Fig. 7, Table 1). While the V$_{oc}$ of the cells using *bis*-PCBM is just slightly lower (0.934 V), a significant drop can be observed for the devices with a-PTCDI (0.897 V).

Photoluminescence (PL) measurements were performed at perovskite films, fabricated with the 1:1:4 (PbI$_2$:PbCl$_2$:MAI) formulation on glass substrates, without and in combination with an ETL layer, PCBM, *bis*-PCBM or a-PTCDI (Fig. 8).

In the presence of the ETLs the emission of the perovskite layer is substaintily quenched indicating an efficient charge transfer from the perovskite to the electron transport material. While the samples with *bis*-PCBM and a-PTCDI exhibit some residual emission, PCBM appears to annihilate the PL of the perovskite almost entirely. This finding correlates with the observed performance trend in the investigated solar cells.

Considering the electron mobility of the ETLs used, PCBM has the highest (5 × 10^{-2} cm^2/Vs) followed by *bis*-PCBM (3 × 10^{-3} cm^2/Vs) (Steiner et al., 2015). From the typical transfer characteristic of a-PTCDI OFET devices fabricated in this work (Fig. S3), a-PTCDI shows typical n-type behavior under positive gate bias, and the electron mobility was found to be 2 × 10^{-6} cm^2/Vs which is lower than that of *bis*-PCBM. Nevertheless a-PTCDI yields a better device performance than *bis*-PCBM. The low J$_{sc}$, observed in *bis*-PCBM devices, might be caused by a bad interface. With PCBM and a-PTCDI the coverage of the irregular perovskite grain boundaries seems better yielding decent J$_{sc}$
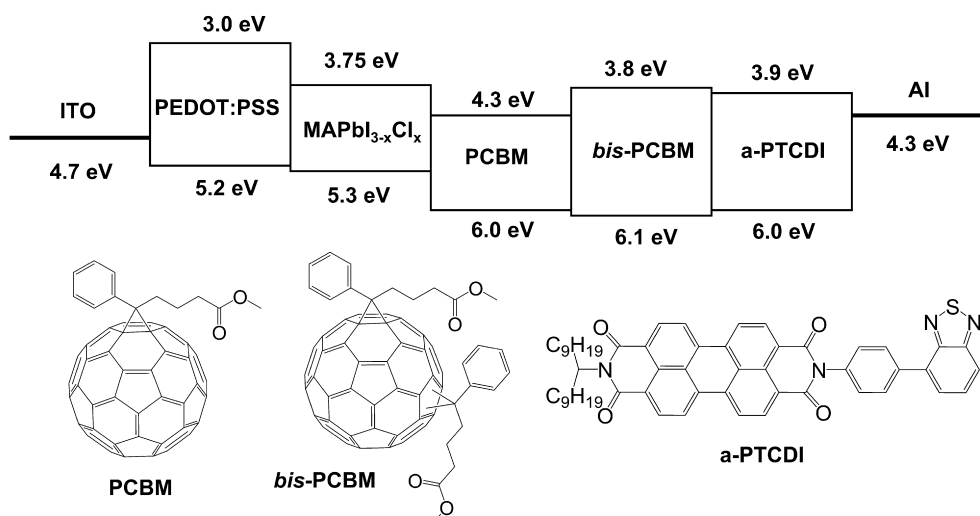

Fig. 6. Schematic of the energy level alignment for the investigated device configuration ITO/PEDOT:PSS/MAPbI$_{3-x}$Cl$_x$/ETL/Al, (*top*), as well as the molecular structures of the ETL materials, PCBM, *bis*-PCBM and a-PTCDI, (*bottom*).
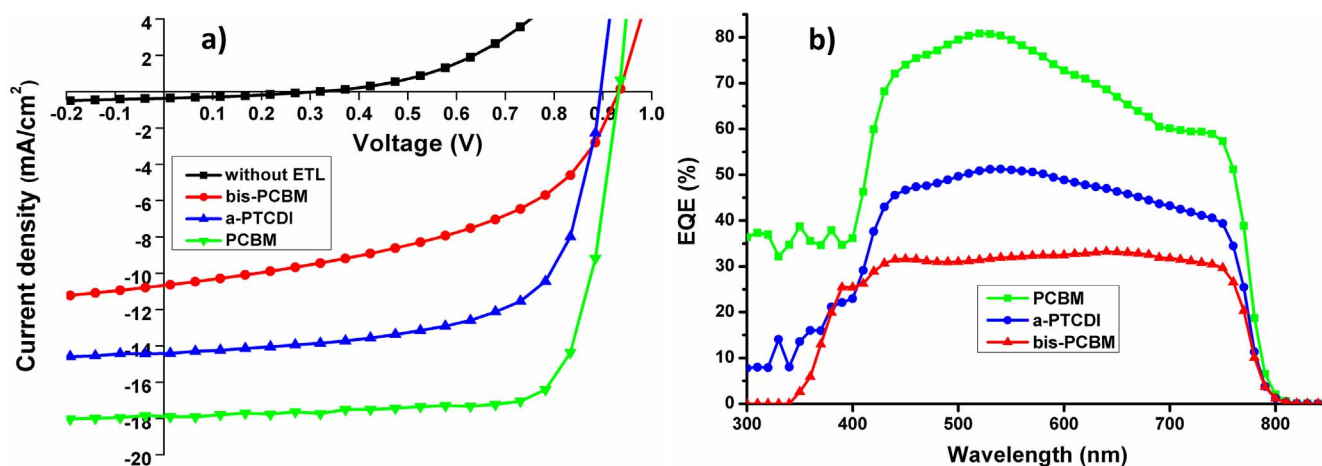
Fig. 7. J-V characteristics of MAPbI$_{3-x}$Cl$_x$ devices without and with ETL (PCBM, *bis*-PCBM or a-PTCDI) (a), and the EQE spectra of the devices with ETL (b).

Table 1
Performance parameters of ITO/PEDOT:PSS/MAPbI$_{3-x}$Cl$_x$/ETL/Al solar cells with different electron transport materials.

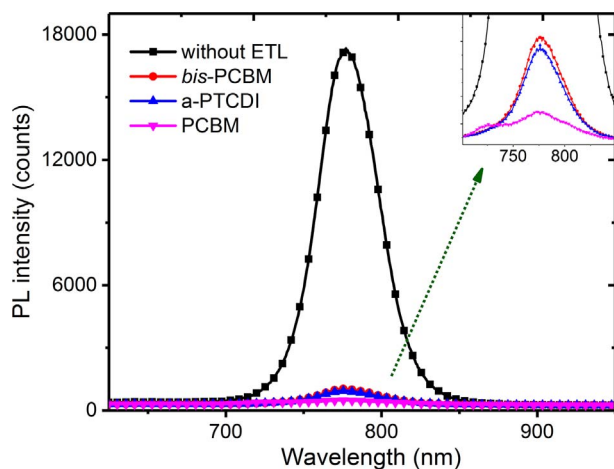| ETL	V$_{oc}$ (V)	J$_{sc}$ (mA/cm^2)	FF	PCE (%)
Without ETL	0.25	0.29	0.31	0.02
bis-PCBM	0.934	10.67	0.48	6.0
a-PTCDI	0.897	14.43	0.65	8.4
PCBM	0.940	17.92	0.76	12.8

Fig. 8. PL spectra of perovskite films prepared on glass substrates from 1:1:4 (PbI$_2$:PbCl$_2$:MAI) precursor solution: without ETL (*black squares*), with *bis*-PCBM layer (*red dots*), with a-PTCDI layer (*blue triangles*) and with PCBM layer (*magenta upside down triangles*). (For interpretation of the references to colour in this figure legend, the reader is referred to the web version of this article.)

numbers (Table 1).

The efficiency of devices with *bis*-PCBM was limited by a much lower FF and J$_{sc}$ inflicted by lower parallel resistance as can be seen from the slope of J-V curves in reverse bias. So we found that the ETL layer quality and its interface property are very critical for achieving high performance. The external quantum efficiency (EQE) spectra of the best-performing perovskite solar cells (PSC) with PCBM, *bis*-PCBM and a-PTCDI as ETL are presented in Fig. 7b. The EQE data corroborate the J-V results and show a gradual decrease, PCBM > a-PTCDI > *bis*-PCBM. The rather poor performance of *bis*-PCBM compared to PCBM is likely to be related to its composition of numerous isomers, which is linked to deficient morphological and energetic order inducing a reduction of the short circuit current density (J$_{sc}$) in polymer solar cells (Bouwer et al., 2012). Isomeric pure *α-bis*-PCBM, however, has been

recently utilized in the preparation of perovskite solar cells, which showed superior characteristics compared to the PCBM-assisted counterparts (Zhang et al., 2017).

A significant challenge in the use of a-PTCDI was, the rather poor film formation by spin coating which made us to use drop casting instead. Even with a rather ill-defined layer of a-PTCDI the solar cells outperformed their counterparts, which used *bis*-PCBM. Improving the processability of a-PTCDI by optimization of its molecular structure and/or the processing parameters could yield devices with significantly enhanced performance.

3.4. Shelf stability

For practical applications, not only the power conversion efficiency but also the stability and lifetime of the photovoltaic device are critical. The environmental stability of perovskite solar cells is affected by the intrinsic instabilities of the perovskite absorber, as well as extrinsic factors which degrade the device as a whole and remains a key challenge to the commercialization of perovskite solar cells. The shelf stability under inert atmosphere (nitrogen-filled glove box) of unencapsulated MAPbI$_3$ perovskite solar cells fabricated from chloride-free precursor formulation (Tombe et al., 2017) and of the best performing CH$_3$NH$_3$PbI$_{3-x}$Cl$_x$ solar cells fabricated from the 1:1:1 (PbI$_2$:MAI:MACl) precursor formulation was monitored over six months. The J-V performance parameters of the devices are shown in Fig. 9 and are summarized in Tables S1 and S2.

The perovskite solar cells are known to be susceptible to moisture ingress (Habisreutinger et al., 2014; Noh et al., 2013), methylammonium iodide egress, (Conings et al., 2015) and corrosion of metal electrodes by the reaction with the halides in the perovskite. The use of a pinhole-free metal oxide layer to prevent metal-halide interaction was reported as a viable approach to enhance stability in PSCs (You et al., 2016).

It is noteworthy that initially the open circuit voltage and the short circuit current density for both devices, MAPbI$_{3-x}$Cl$_x$ and MAPbI$_3$, exhibit relatively small losses over time. The reduction in fill factor, on the other hand, appears as the primary symptom of the device degradation (Fig. 9, Tables S1 and S2). Both MAPbI$_3$ and MAPbI$_{3-x}$Cl$_x$ perovskite solar cells showed distinct sign of aging without encapsulation or any special protection displaying irreversible degradation, most likely due to traces of moisture in the glove box atmosphere.

After 6 months, the MAPbI$_3$ device retained 33% of its original power conversion efficiency whereas the MAPbI$_{3-x}$Cl$_x$ device retained 50%, reflected in reduced FF and J$_{sc}$ (Tables S1 and S2). This might be also indicative for the hygroscopic nature of PEDOT:PSS, which can induce degradation of ITO (de Jong et al., 2000) and decomposes the
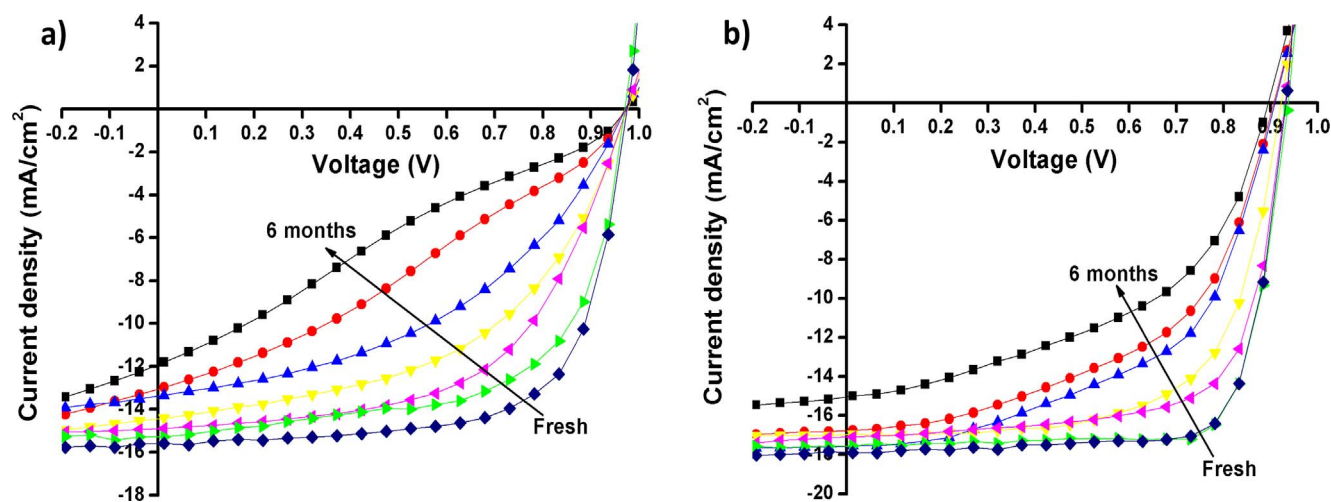
Fig. 9. J-V response under AM1.5G illumination for typical freshly-prepared and aged glass/ITO/PEDOT:PSS/perovskite/PCBM/Al solar cells, (a) MAPbI$_3$ and (b) MAPbI$_{3-x}$Cl$_x$ kept in glove box (N$_2$) and measured once per month over the course of six months.

perovskite absorber layer. It is interesting that the V_{oc} is not much influenced by the degradation, while the reduced J_{sc} and FF are affecting the final performance significantly in both MAPbI$_3$ and MAPbI$_{3-x}$Cl$_x$ devices. Both MAPbI$_3$ and MAPbI$_{3-x}$Cl$_x$ might undergo a similar moisture-assisted degradation process in which methylamine is lost leaving PbI$_2$ behind. (Philippe et al., 2015) The formation of dense uniform MAPbI$_{3-x}$Cl$_x$ perovskite films with large crystal domains in this work might cause the enhanced stability observed in MAPbI$_{3-x}$Cl$_x$ devices compared to MAPbI$_3$ cells.

4. Conclusion

Seeking to understand and improve the performance of perovskite solar cells fabricated in a straight forward fashion, we demonstrated that overall ion composition of precursor formulation has a critical influence on the perovskite crystallization and film morphology while the components by which these ions are introduced, lead and/or methylammonium halides, seem non-relevant. The apparent correlation between device performance and perovskite grain size shows, that large (micrometer-sized) grains are an important morphological feature of high efficient perovskite solar cells. The presence of a suitable non stoichometric amount of MACl in the perovskite formulations 1:1:1 (PbI$_2$:MAI:MACl) and 1:1:4 (PbI$_2$:PbCl$_2$:MAI), facilitates favorable crystallization dynamics in ambient atmosphere. Rather high amounts of MACl, in 1:3 (PbCl$_2$:MAI) formulation, however, appear to yield perovskite layers with poor morphology and device performance under the used conditions. Furthermore, an electron transport layer between perovskite and low work function electrode proofed to be essential for our cell design, glass/ITO/PEDOT:PSS/perovskite/ETL/Al, for better charge extraction, to inhibit electrode corrosion and perovskite degradation. Out of the three solution-processable electron acceptor materials tested, PCBM, *bis*-PCBM and an amorphous a-PTCDI, PCBM provided the best performance due to a favorable interface and energy level alignment promoting effective electron transfer and low probability for charge recombination.

Perovskite solar cells prepared in absence of MACl (purly PbMAI$_3$ formulation) showed quite good performance initially, but significantly lower shelf live time compared to the devices fabricated with the mixed-halide MAPbI$_{3-x}$Cl$_x$ perovskite formulation. The realization of practical goals such as commercialization of perovskite solar cells will be strongly determined by a detailed understanding of the roles played by perovskite chemistry, crystallization dynamics, the effects of processing parameters, key materials employed in perovskite device layers and the achievable stability.

Appendix A. Supplementary material

Supplementary data associated with this article can be found, in the online version, at http://dx.doi.org/10.1016/j.solener.2018.01.083.

References

Adam, G., Kaltenbrunner, M., Głowacki, E.D., Hazar, D.H., White, M.S., Heilbrunner, H., Tombe, S., Stadler, P., Ernecker, B., Klampfl, C.W., Sariciftci, N.S., Scharber, M.C., 2016. Solution processed perovskite solar cells using highly conductive PEDOT:PSS interfacial layer. Sol. Energy Mater. Sol. Cells 157, 318–325.

Bailey, Z.M., McGehee, M.D., 2012. Modeling low cost hybrid tandem photovoltaics with the potential for efficiencies exceeding 20%. Energy Environ. Sci. 5, 9173–9179.

Ball, J.M., Lee, M.M., Hey, A., Snaith, H.J., 2013. Low-temperature processed meso-superstructured to thin-film perovskite solar cells. Energy Environ. Sci. 6, 1739.

Barrows, A.T., Pearson, A.J., Kwak, C.K., Dunbar, A.D.F., Buckley, A.R., Lidzey, D.G., 2014. Efficient planar heterojunction mixed-halide perovskite solar cells deposited via spray-deposition. Energy Environ. Sci. 7, 2944–2950.

Bouwer, R.K.M., Wetzelaer, G.J.A.H., Blom, P.W.M., Hummelen, J.C., 2012. Influence of the isomeric composition of the acceptor on the performance of organic bulk heterojunction P3HT:bis-PCBM solar cells. J. Mater. Chem. 22, 15412–15417.

Burschka, J., Pellet, N., Moon, S.-J., Humphry-Baker, R., Gao, P., Nazeeruddin, M.K., Grätzel, M., 2013. Sequential deposition as a route to high-performance perovskite-sensitized solar cells. Nature 499, 316–319.

Chen, Q., Zhou, H., Hong, Z., Luo, S., Duan, H.-S., Wang, H.-H., Liu, Y., Li, G., Yang, Y., 2014. Planar heterojunction perovskite solar cells via vapor-assisted solution process. J. Am. Chem. Soc. 136, 622–625.

Conings, B., Drijkoningen, J., Gauquelin, N., Babayigit, A., D'Haen, J., Olieslaeger, L.D'., Ethirajan, A., Verbeeck, J., Manca, J., Mosconi, E., De Angelis, F., Boyen, H.-G., 2015. Intrinsic thermal instability of methylammonium lead trihalide perovskite. Adv. Energy Mater. 5, 1500477.

Correa Baena, J.P., Steier, L., Tress, W., Saliba, M., Neutzner, S., Matsui, T., Giordano, F., Jacobsson, T.J., Kandada, A.R.S., Zakeeruddin, S.M., Petrozza, A., Abate, A., Nazeeruddin, M.K., Grätzel, M., Hagfeldt, A., 2015. Highly efficient planar perovskite solar cells through band alignment engineering. Energy Environ. Sci. 8, 2928–2934.

Cui, P., Wei, D., Ji, J., Song, D., Li, Y., Liu, X., Huang, J., Wang, T., You, J., Li, M., 2017. Highly efficient electron-selective layer free perovskite solar cells by constructing effective p–n heterojunction. Sol. RRL 1, 1600027.

de Jong, M.P., van IJzendoorn, L.J., de Voigt, M.J.A., 2000. Stability of the interface

between indium-tin-oxide and poly(3,4-ethylenedioxythiophene)/poly(styrenesulfonate) in polymer light-emitting diodes. Appl. Phys. Lett. 77, 2255.

Docampo, P., Ball, J.M., Darwich, M., Eperon, G.E., Snaith, H.J., 2013. Efficient organometal trihalide perovskite planar-heterojunction solar cells on flexible polymer substrates. Nat. Commun. 4, 2761.

Eperon, G.E., Burlakov, V.M., Docampo, P., Goriely, A., Snaith, H.J., 2014b. Morphological control for high performance, solution-processed planar heterojunction perovskite solar cells. Adv. Funct. Mater. 24, 151–157.

Eperon, G.E., Stranks, S.D., Menelaou, C., Johnston, M.B., Herz, L.M., Snaith, H.J., 2014a. Formamidinium lead trihalide: a broadly tunable perovskite for efficient planar heterojunction solar cells. Energy Environ. Sci. 7, 982–988.

Etgar, L., Gao, P., Xue, Z., Peng, Q., Chandiran, A.K., Liu, B., Nazeeruddin, M.K., Grätzel, M., 2012. Mesoscopic CH₃NH₃PbI₃/TiO₂ heterojunction solar cells. J. Am. Chem. Soc. 134, 17396–17399.

Habisreutinger, S.N., Leijtens, T., Eperon, G.E., Stranks, S.D., Nicholas, R.J., Snaith, H.J., 2014. Carbon nanotube/polymer composites as a highly stable hole collection layer in perovskite solar cells. Nano Lett. 14, 5561–5568.

Han, G.D., Maurano, A., Weis, J.G., Bulovic, V., Swager, T.M., 2016. Voc enhancement in polymer solar cells with isobenzofulvene-C60 adducts. Org. Electron. 31, 48–55.

He, Y., Li, Y., 2011. Fullerene derivative acceptors for high performance polymer solar cells. PCCP 13, 1970–1983.

Heo, J.H., Im, S.H., 2016. Highly reproducible, efficient hysteresis-less CH₃NH₃PbI₃₋ₓClₓ planar hybrid solar cells without requiring heat-treatment. Nanoscale 8, 2554–2556.

Huang, C., Barlow, S., Marder, S.R., 2011. Perylene-3,4,9,10-tetracarboxylic acid diimides: synthesis, physical properties, and use in organic electronics. J. Org. Chem. 76, 2386–2407.

Jeon, N.J., Noh, J.H., Kim, Y.C., Yang, W.S., Ryu, S., Seok, S.I., 2014. Solvent engineering for high-performance inorganic-organic hybrid perovskite solar cells. Nat. Mater. 13, 897–903.

Jeon, N.J., Noh, J.H., Yang, W.S., Kim, Y.C., Ryu, S., Seo, J., Seok, S.I., 2015. Compositional engineering of perovskite materials for high-performance solar cells. Nature 517, 476–480.

Kagan, C.R., Mitzi, D.B., Dimitrakopoulos, C.D., 1999. Organic-inorganic hybrid materials as semiconducting channels in thin-film field-effect transistors. Science 286, 945–947.

Kaltenbrunner, M., Adam, G., Głowacki, E.D., Drack, M., Schwödiauer, R., Leonat, L., Hazar, D.H., Groiss, H., Scharber, M.C., White, M.S., Sariciftci, N.S., Bauer, S., 2015. Flexible high power-per-weight perovskite solar cells with chromium oxide-metal contacts for improved stability in air. Nat. Mater. 14, 1032–1039.

Ke, W., Fang, G., Wan, J., Tao, H., Liu, Q., Xiong, L., Qin, P., Wang, J., Lei, H., Yang, G., 2015. Efficient hole-blocking layer-free planar halide perovskite thin-film solar cells. Nat. Commun. 6, 6700.

Kim, H.-B., Choi, H., Jeong, J., Kim, S., Walker, B., Song, S., Kim, J.Y., 2014. Mixed solvents for the optimization of morphology in solution-processed, inverted-type perovskite/fullerene hybrid solar cells. Nanoscale 6, 6679–6683.

Kim, H.-S., Lee, C.-R., Im, J.-H., Lee, K.-B., Moehl, T., Marchioro, A., Moon, S.-J., Humphry-Baker, R., Yum, J.-H., Moser, J.E., Grätzel, M., Park, N.-G., 2012. Lead iodide perovskite sensitized all solid-state submicron thin film mesoscopic solar cell with efficiency exceeding 9%. Sci. Rep. 2, 591.

Kim, H.-S., Park, N.-G., 2014. Parameters affecting I–V hysteresis of CH₃NH₃PbI₃ perovskite solar cells: Effects of perovskite crystal size and mesoporous TiO₂ Layer. J. Phys. Chem. Lett. 5, 2927–2934.

Kim, J., Teridi, M.A., bin Mohd Yusoff, A.R., Jang, J., 2016. Stable and null current hysteresis perovskite solar cells based nitrogen doped graphene oxide nanoribbons hole transport layer. Sci. Rep. 6, 27773.

Ko, H.-S., Lee, J.-W., Park, N.-G., 2015. 15.76% efficiency perovskite solar cells prepared under high relative humidity: Importance of PbI₂ morphology in two-step deposition of CH₃NH₃PbI₃. J. Mater. Chem. A 3, 8808–8815.

Kojima, A., Masashi, I., Kenyiro, T., Totsumo, M., 2012. Highly luminescent lead bromide perovskite nanoparticles synthesized with porous alumina media. Chem. Lett. 41, 397–399.

Langhals, H., Knochel, P., Walter, A., Simdras, S., 2012. Benzothiadiazoloperylenes and benzoxadiazoloperylenes: Amorphous functional materials. Synthesis 44, 3465–3477.

Lee, J.-W., Kim, D.-H., Kim, H.-S., Seo, S.-W., Cho, S.M., Park, N.-G., 2015. Formamidinium and cesium hybridization for photo-and moisture-stable perovskite solar cell. Adv. Energy Mater. 5, 1501310.

Lee, M.M., Teuscher, J., Miyasaka, T., Murakami, T.N., Snaith, H.J., 2012. Efficient hybrid solar cells based on meso-superstructured organometal halide perovskites. Science 338, 643–647.

Lenes, M., Wetzelaer, G.-J.A.H., Kooistra, F.B., Veenstra, S.C., Hummelen, J.C., Blom, P.W.M., 2008. Fullerene bisadducts for enhanced open-circuit voltages and efficiencies in polymer solar cells. Adv. Mater. 20, 2116–2119.

Liang, P.-W., Liao, C.-Y., Chueh, C.-C., Zuo, F., Williams, S.T., Xin, X.-K., Lin, J., Jen, A.K.Y., 2014. Additive enhanced crystallization of solution-processed perovskite for highly efficient planar-heterojunction solar cells. Adv. Mater. 26, 3748–3754.

Liu, M., Johnston, M.B., Snaith, H.J., 2013. Efficient planar heterojunction perovskite solar cells by vapour deposition. Nature 501, 395–398.

Löper, P., Stuckelberger, M., Niesen, B., Werner, J., Filipič, M., Moon, S.-J., Yum, J.-H., Topič, M., De Wolf, S., Ballif, C., 2015. Complex refractive index spectra of CH₃NH₃PbI₃ perovskite thin films determined by spectroscopic ellipsometry and spectrophotometry. J. Phys. Chem. Lett. 6, 66–71.

Malinkiewicz, O., Yella, A., Lee, Y.H., Espallargas, G.M., Grätzel, M., Nazeeruddin, M.D., Bolink, H.J., 2014. Perovskite solar cells employing organic charge-transport layers. Nat. Photon. 8, 128–132.

Manser, J.S., Reid, B., Kamat, P.V., 2015. Evolution of organic–inorganic lead halide perovskite from solid-state iodoplumbate complexes. J. Phys. Chem. C. 119, 17065–17073.

Manser, J.S., Saidaminov, M.I., Christians, J.A., Bakr, O.M., Kamat, P.V., 2016. Making and breaking of lead halide perovskites. Acc. Chem. Res. 49, 330–338.

Mei, A., Li, X., Liu, L., Ku, Z., Liu, T., Rong, Y., Xu, M., Hu, M., Chen, J., Yang, Y., Grätzel, M., Han, H., 2014. A hole-conductor-free, fully printable mesoscopic perovskite solar cell with high stability. Science 345, 295–298.

Mitzi, D.B., Field, C.A., Schlesinger, Z., Laibowitz, R.B., 1995. Transport, optical, and magnetic properties of the conducting halide perovskite CH₃NH₃SnI₃. J. Solid State Chem. 114, 159–163.

Nie, W., Tsai, H., Asadpour, R., Blancon, J.-C., Neukirch, A.J., Gupta, G., Crochet, J.J., Chhowalla, M., Tretiak, S., Alam, M.A., Wang, H.-L., Mohite, A.D., 2015. High-efficiency solution processed perovskite solar cells with millimeter-scale grains. Science 347, 522–525.

Noh, J.H., Im, S.H., Heo, J.H., Mandal, T.N., Seok, S.I., 2013. Chemical management for colorful, efficient, and stable inorganic-organic hybrid nanostructured solar cells. Nano Lett. 13, 1764–1769.

Philippe, B., Park, B.-W., Lindblad, R., Oscarsson, J., Ahmadi, S., Johansson, E.M.J., Rensmo, H., 2015. Chemical and electronic structure characterization of lead halide perovskites and stability behavior under different exposures – A photoelectron spectroscopy investigation. Chem. Mater. 27, 1720–1731.

Poglitsch, A., Weber, D., 1987. Dynamic disorder in methylammonium-trihalogenoplumbates (II) observed by millimeter-wave spectroscopy. J. Chem. Phys 87, 6373–6378.

Roldán-Carmona, C., Malinkiewicz, O., Soriano, A., Espallargas, G.M., Garcia, A., Reinecke, P., Kroyer, T., Dar, M.I., Nazeeruddin, M.K., Bolink, H.J., 2014. Flexible high efficiency perovskite solar cells. Energy Environ. Sci. 7, 994–997.

Saliba, M., Matsui, T., Seo, J.-Y., Correa-Baena, J.-P., Nazeeruddin, M.K., Zakeeruddin, S.M., Tress, W., Abate, A., Hagfeldt, A., Grätzel, M., 2016. Cesium-containing triple cation perovskite solar cells: improved stability, reproducibility and high efficiency. Energy. Environ. Sci. 9, 1989–1997.

Saliba, M., Tan, K.W., Sai, H., Moore, D.T., Scott, T., Zhang, W., Estroff, L.A., Wiesner, U., Snaith, H.J., 2014. Influence of thermal processing protocol upon the crystallization and photovoltaic performance of organic–inorganic lead trihalide perovskites. J. Phys. Chem. C. 118, 17171–17177.

Steiner, F., Foster, S., Losquin, A., Labram, J., Anthopoulos, T.D., Frost, J.M., Nelson, J., 2015. Distinguishing the influence of structural and energetic disorder on electron transport in fullerene multi-adducts. Mater. Horiz. 2, 113–119.

Stranks, S.D., Eperon, G.E., Grancini, G., Menelaou, C., Alcocer, M.J.P., Leijtens, T., Herz, L.M., Petrozza, A., Snaith, H.J., 2013. Electron-hole diffusion lengths exceeding 1 micrometer in an organometal trihalide perovskite absorber. Science 342, 341–344.

Sun, S., Salim, T., Mathews, N., Duchamp, M., Boothroyd, C., Xing, G., Sum, T.C., Lam, Y.M., 2014. The origin of high efficiency in low-temperature solution-processable bilayer organometal halide hybrid solar cells. Energy Environ. Sci. 7, 399–407.

Sutherland, B.R., Hoogland, S., Adachi, M.M., Kanjanaboos, P., Wong, C.T., McDowell, J.J., Voznyy, J., Xu, O., Ning, Z., Houtepen, A.J., Sargent, E.H., 2015. Perovskite thin films via atomic layer deposition. Adv. Mater. 27, 53–58.

Tombe, S., Adam, G., Heilbrunner, H., Apaydin, D.H., Ulbricht, C., Sariciftci, N.S., Arendse, C.J., Iwuoha, E., Scharber, M.C., 2017. Optical & electrical properties of mixed halide (X= Cl, Br, I) methylammonium perovskite solar cells. J. Mater. Chem. C 5, 1714–1723.

Wei, Z., Chen, H., Yan, K., Yang, S., 2014. Inkjet printing and instant chemical transformation of a CH₃NH₃PbI₃/nanocarbon electrode and interface for planar perovskite solar cells. Angew. Chem. 53, 13239–13243.

Xiao, Z.G., Bi, C., Shao, Y.C., Dong, Q.F., Wang, Q., Yuan, Y.B., Wang, C.G., Gao, Y.L., Huang, J.S., 2014. Efficient, high yield perovskite photovoltaic devices grown by interdiffusion of solution-processed precursor stacking layers. Energy Environ. Sci. 7, 2619–2623.

Yang, M., Zhou, Y., Zeng, Y., Jiang, C.-S., Padture, N.P., Zhu, K., 2015. Square-centimeter solution processed planar CH₃NH₃PbI₃ perovskite solar cells with efficiency exceeding 15%. Adv. Mater. 27, 6363–6370.

Yang, W.S., Noh, J.H., Jeon, N.J., Kim, Y.C., Ryu, S., Seo, J., Seok, S.I., 2015. High-performance photovoltaic perovskite layers fabricated through intramolecular exchange. Science 348, 1234–1237.

Yang, Z., Chueh, C.-C., Liang, P.-W., Crump, M., Lin, F., Zhu, Z., Jen, A.K.-Y., 2016. Effects of formamidinium and bromide ion substitution in methylammonium lead triiodide toward high-performance perovskite solar cells. Nano Energy 22, 328–337.

Ye, L., Zhang, S., Qian, D., Wang, Q., Hou, J., 2013. Application of bis-PCBM in polymer solar cells with improved voltage. J. Phys. Chem. C 117, 25360–25366.

Yin, W., Pan, L., Yang, T., Liang, Y., 2016. Recent advances in interface engineering for planar heterojunction perovskite solar cells. Molecules 21, 837.

You, J., Yang, Y., Hong, Z., Song, T.-B., Meng, L., Liu, Y., Jiang, C., Zhou, H., Chang, W.-H., Li, G., Yang, Y., 2014. Moisture assisted perovskite film growth for high performance solar cells. J. Appl. Phys. 105, 183902.

You, J., Meng, L., Song, T.-B., Guo, T.-F., Yang, Y.(M), Chang, W.-H., Hong, Z., Chen, H., Zhou, H., Chen, Q., Liu, Y., De Marco, N., Yang, Y., 2016. Improved air stability of perovskite solar cells via solution-processed metal oxide transport layers. Nat. Nanotechnol. 11, 75–81.

Zhan, X., Facchetti, A., Barlow, S., Marks, T.J., Ratner, M.A., Wasielewski, M.R., 2011. Rylene and related diimides for organic electronics. Adv. Mater. 23, 268–284.

Zhang, Y., Hu, X., Chen, L., Huang, Z., Fu, Q., Liu, Y., Zhang, L., Chen, Y., 2016. Flexible, hole transporting layer-free and stable CH₃NH₃PbI₃/PC₆₁BM planar heterojunction Perovskite solar cells. Org. Electron. 30, 281–288.

Zhang, F., Shi, W., Luo, J., Pellet, N., Yi, C., Li, X., Zhao, X., Dennis, T.J.S., Li, X., Wang, S., Xiao, Y., Zakeeruddin, S.M., Bi, D., Grätzel, M., 2017. Isomer-pure bis-PCBM-assisted crystal engineering of perovskite solar cells showing excellent efficiency and stability. Adv. Mater. 29, 1606806.

Zhao, Y., Zhu, K., 2014. Solution chemistry engineering toward high-efficiency perovskite solar cells. J. Phys. Chem. Lett. 5, 4175–4186.